INTERNATIONAL JOURNAL FOR NUMERICAL METHODS IN FLUIDS
Int. J. Numer. Meth. Fluids 2003; **41**:389–417 (DOI: 10.1002/fld.446)

Estimating zero-g flow rates in open channels having capillary pumping vanes

Radhakrishnan Srinivasan*,†

R&D Group—Exports Services, IBM Global Services India Pvt. Ltd., 5th Floor, Golden Enclave, Airport Road, Bangalore 560017, India

SUMMARY

In vane-type surface tension propellant management devices (PMD) commonly used in satellite fuel tanks, the propellant is transported along guiding vanes from a reservoir at the inlet of the device to a sump at the outlet from where it is pumped to the satellite engine. The pressure gradient driving this free-surface flow under zero-gravity (zero-g) conditions is generated by surface tension and is related to the differential curvatures of the propellant-gas interface at the inlet and outlet of the PMD. A new semi-analytical procedure is prescribed for accurately calculating the extremely small fuel flow rates under reasonably idealized conditions. Convergence of the algorithm is demonstrated by detailed numerical calculations. Owing to the substantial cost and the technical hurdles involved in accurately estimating these minuscule flow rates by either direct numerical simulation or by experimental methods which simulate zero-g conditions in the lab, it is expected that the proposed method will be an indispensable tool in the design and operation of satellite fuel tanks. Copyright © 2003 John Wiley & Sons, Ltd.

KEY WORDS: zero-g; propellant flow rates; capillary pumping vanes; stokes flow; semi-analytical solution

1. INTRODUCTION

In a vane-type surface tension propellant management device (PMD), commonly used in satellite fuel tanks, liquid propellant is transported along open channel vanes from an inlet reservoir to a sump (propellant trap) located at the outlet of the device, from where it is pumped to the satellite engine. The salient features of this device are illustrated in the idealized geometry shown in Figure 1, where all quantities in upper case are dimensional. Here the reservoir and the sump are taken as identical conical sections (of revolution) and the vane and fuel tank wall are assumed to be straight in the flow direction X. In actual practice the fuel tank would be typically spherical or elongate and the inlet and outlet compartment geometries more complex. Some of the design features of these vane-type fuel tanks are described in the patent literature [1–4]. Under zero gravity (zero-g) conditions, the pressure gradient driving the flow

*Correspondence to: R. Srinivasan, R&D Group—Exports Services, IBM Global Services India Pvt. Ltd., 5th Floor, Golden Enclave, Airport Road, Bangalore, 560017, India.
†E-mail: sradhakr@in.ibm.com

Received June 2001
Revised 15 July 2002

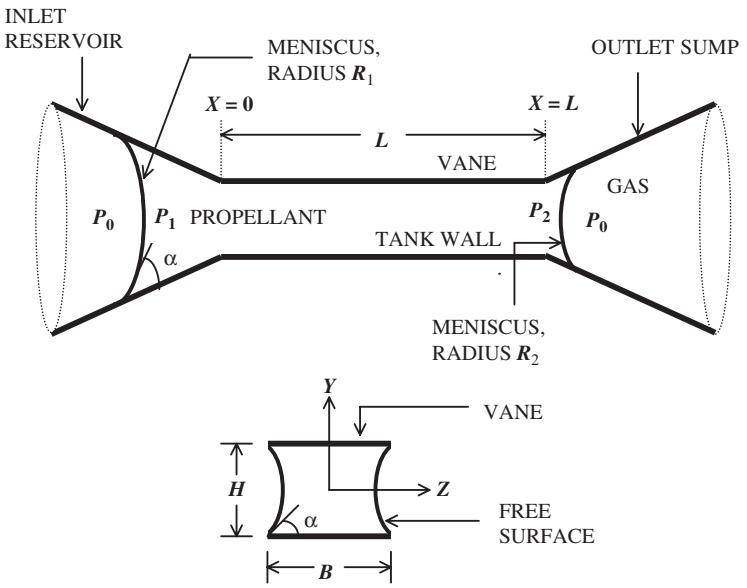

Figure 1. The flow geometry and co-ordinate system.

in the positive X direction is generated by surface tension and is related to the difference in the curvatures of the gas-propellant interfaces at the reservoir and the sump respectively. In Figure 1, the pressure jumps discontinuously from the ambient P_0 to the fluid pressure P_1 across the inlet interface and from P_0 to P_2 across that at the outlet; these discontinuities are determined by the well-known Laplace–Young equation. The pressure differential driving the flow is then given by $P_1 - P_2$. In the situation shown in Figure 1, the contact angle α satisfies $0 \leqslant \alpha < \pi/2$, corresponding to a wetting fluid (which is the case for most propellants) and $P_1 - P_2$ would be positive provided the radius of curvature of the inlet interface exceeds that of the outlet.

In a real-life situation, after one set of satellite orbiting maneuvers are completed, the designer/operator would like to know for how long one has to wait before the sump gets refilled, so that the next set of maneuvers may be performed. Given the complexity of the governing equations in this free-surface flow problem, the only possible options are to generate the required data for the drainage times either experimentally or via numerical simulation. If one decides to proceed experimentally, the options are to either perform the experiment in space (which would obviously be expensive) or on the ground, where one would be faced with the cost and difficulties of setting up a zero-g environment. Some of the other issues involved in an experimental scenario are discussed in References [5, 9]. The second option, of using computer simulation, presents equally difficult challenges. One has to compute an unsteady, three-dimensional free-surface flow in a complex geometry. Further, the flow rates involved in a zero-g environment are extremely small; typically, the drainage time for 2 l of propellant could be anywhere from 8 to 24 h. These flow rates are several orders of magnitude less than those in a 1-g environment. Computing these zero-g flows by a direct unsteady 3-D simulation would not only be prohibitively expensive; the issues of convergence and accuracy

would be difficult to settle because of the extremely small flow rates involved. If one attempts to take care of the complexity of the geometry by ignoring the entry and exit regions, then the problem would be to accurately estimate the entry and exit conditions in a straight section of the vane. The author is not aware of direct numerical simulation results for a zero-g PMD published in the open or patent literature; estimates of drainage times are available ([6–9]). In particular, Ducret *et al.* [9] estimate a vane flow rate of $0.4\,\mathrm{cm}^3/\mathrm{s}$ 'for the worst case situation of the input parameters', although the details of their method are not given. A more detailed discussion of the difficulties associated with a full-fledged numerical simulation, versus the advantages of the present approach, is given in Section 5.

Prior to the present paper, the only published theoretical estimates of the flow rates are due to Jaekle [10] and subsequent improvements by Dreyer and co-workers [11–13]. This method uses an integral analysis of the continuity and momentum equations with an averaged velocity in the flow direction and neglects cross flows. The friction losses are estimated heuristically. The radius of curvature $R(X)$ of the free surface is assumed constant at any location X in the flow direction and the integral analysis yields a non-linear differential equation for $\mathrm{d}R/\mathrm{d}X$ as a function of X, R and certain other parameters. Further, the contact angle condition is ignored by these authors, unlike in the present work. Their method can handle non-zero Reynolds numbers, but is certainly cruder as compared to that presented in this paper for the Stokes flow case.

In this paper, a novel semi-analytical procedure is proposed to accurately and economically calculate the fuel flow rates in a zero-g PMD under certain reasonably idealized conditions. Because the technique uses exact analytical solutions (via eigenfunction expansions) of a suitably perturbed version of the Stokes flow equations, the issue of convergence is confined to the accuracy with which boundary data are satisfied. The contact angle condition and cross flows are not ignored and the viscous losses are a result of the analysis. Further, because of the small computer times and memory requirements, one is able to easily study the effect of parameters in the problem, such as, aspect ratio and contact angle. In the ensuing sections, the idealizations involved and the formulation are explained; the numerical algorithm is briefly discussed; and numerical convergence results are presented for a range of values of the parameters. The only data available in the literature for the flow rates are in [11–13]; unfortunately, these are for non-zero Reynolds numbers and the lengths of the devices used were not large enough for the assumption of slow variation in X required by our method. Nevertheless, some comparisons are given in Section 8.

2. FORMULATION

2.1. Idealization of the geometry

As we have seen in Section 1, the geometry of Figure 1 is already an idealized version in the sense that the vane is assumed to be straight in the flow direction (X) and that the inlet and exit compartments are simplified to be conical sections of revolution. The latter assumption is not essential for our analysis and is made only for convenience; in conical sections, the meniscus curvature for a given volume of contained fuel and the rate of change of this curvature for a given drainage/accumulation rate of the contained fuel are both easily calculated analytically, while in a more complicated geometry one would have to obtain these

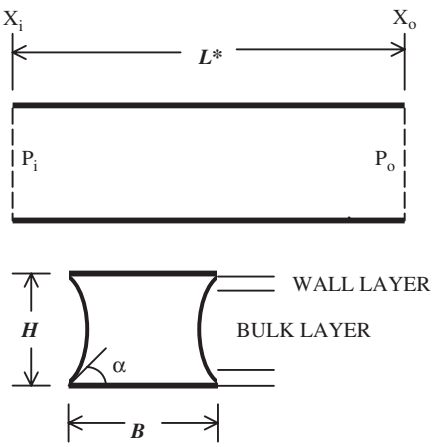

Figure 2. A portion of the channel in Figure 1.

quantities by numerical quadrature/differentiation. Neglect of the vane curvature is justified as follows. In practice, the fuel tank wall is spherical and the vanes guide the fuel along this wall from the inlet to the outlet compartments. The ratio of the radius of curvature of the tank wall to the height of the channel cross section (H in Figure 1) is usually large, of the order of several hundreds. Secondly, because of the extremely small flow rates involved, it is expected that the acceleration effects due to small curvature in the flow direction can be safely neglected to leading order; as we will shortly see, fluid inertia is already a higher-order effect in our analysis because of the small Reynolds numbers.

We now describe the crucial steps in idealization of the geometry, which enable us to proceed analytically. In actual practice, the length L of the channel is large, typically of the order of $100H$. This suggests that the flow at locations far away from the entry and exit regions would be 'fully developed', that is, independent (to leading order) of the actual conditions prevalent at the inlet and outlet of the device. Thus one may analyze the fully developed flow in a straight segment of length L^* which is still assumed to be large compared to H, but whose entry and exit points are 'far away' from the entry and exit regions of the actual device shown in Figure 1; in conclusion, the flow in the geometry of Figure 2 is to be analysed, where

$$L^*/H \to \infty, \quad X_i/H \to \infty, \quad (L - X_o)/H \to \infty$$

We have seen that the flow rates are extremely small because of the small pressure differentials driving the flow. Therefore, as will be shortly seen, the 'quasi-steady' approximation is made: the time derivatives drop out to leading order in a suitably non-dimensionalized version of the governing equations. The flow rate in the device of Figure 2 would depend only on the (instantaneous) pressure gradient, which itself changes slowly with time. This pressure gradient may be obtained as follows. Let the radii of curvature of the meniscus at the inlet and outlet compartments be R_1 and R_2 at some given instant, as shown in Figure 1. Given the volumes of fluid at the inlet/outlet compartments and the contact angle α (which is a thermodynamic parameter dependent only on the propellant and the material of the PMD,

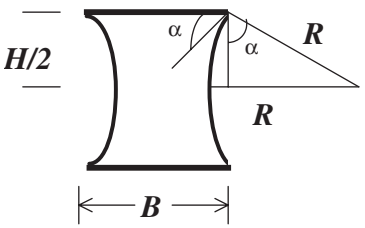

Figure 3. The static case (no flow).

usually titanium or stainless steel), R_1 and R_2 may be easily calculated. The Laplace–Young equation relates the ambient pressure P_0 to the fluid pressure P as follows:

$$P_0 - P = \sigma \left[\frac{1}{R_a} + \frac{1}{R_b} \right] \tag{1}$$

where R_a and R_b are the principal radii of curvature in two mutually perpendicular directions and σ is the surface tension coefficient. Using this formula, one may obtain the instantaneous pressure difference for the device of Figure 1 as follows:

$$P_1 - P_2 = 2\sigma \left[\frac{1}{R_2} - \frac{1}{R_1} \right] \tag{2}$$

Because the velocity of the fluid is very small, one may, upon using Bernoulli's equation, neglect the pressure drops across the inlet/exit compartments and conclude that the pressure drop across the channel of length L in Figure 1 is $P_1 - P_2$. We now assume that the entry/exit regions are very small compared to the length of the device and may therefore be neglected; that is, the flow is 'fully developed' over most of the length L. This is an excellent approximation because the length L is very large compared to H and the flow rates/pressure gradients are very small. One may therefore approximate $L^* \approx L$ without significant loss of accuracy and take the (instantaneous) leading-order pressures at the inlet and outlet of the device of Figure 2 to be P_1 and P_2, respectively. The problem now is to figure out the flow rate at this instant; to repeat this calculation for various other pressure drops till the inlet/outlet pressures in Figure 1 equalize (that is, the meniscus radii satisfy $R_1 = R_2$); finally determine the total drainage time by integration.

Having fixed the length and the leading-order inlet/outlet pressures in the device, the crucial issue of the shape of the free surface is addressed next, so that one may proceed with the flow rate calculation. To gain some insight, first consider the static case when the inlet and outlet pressures in Figure 2 are equal and there is no flow. The free surface (at any given location X) in this case is shown in Figure 3 and has the shape of an arc of a circle, because the pressure across the entire cross-section must be uniform. Further, the contact angle α must be maintained and this gives the radius of curvature of the free surface in

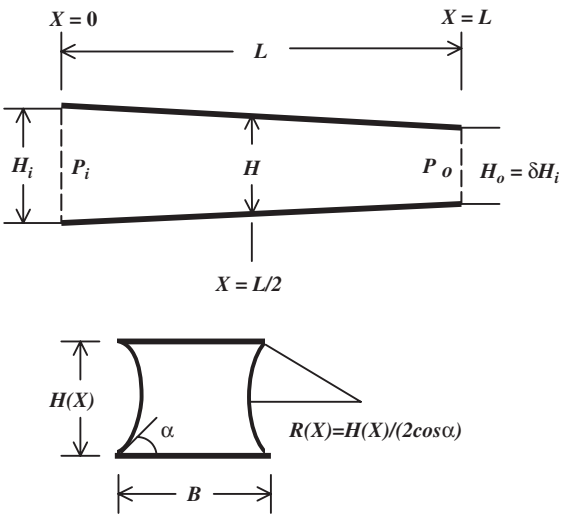

Figure 4. Idealized geometry with linear gradient in channel height.

Figure 3 as

$$R = \frac{H}{2\cos\alpha} \tag{3}$$

Now consider the situation in which there is a small steady pressure gradient and therefore a small flow rate in Figure 2. Intuitively, one feels that the free surface shape will still tend to be 'nearly circular'; in other words, the pressure will not vary much across most of the cross section in Figure 3, at any given location X. Further, assuming that the solid surfaces are highly polished, the contact angle must still be maintained. The only way to reconcile these two requirements is to assume that the free surface is circular (to leading order) everywhere except for small layers near the walls, where the contact angle requirement would force a deviation. The radius of curvature of this circular part at any instant of time will be determined by the corresponding leading-order pressure at any given location X and the Laplace–Young equation. In general, the analysis of the wall-layers would be cumbersome analytically. The question that naturally arises is whether the (instantaneous) flow rates can be estimated without having to deal with these layers. If one ignores the contact angle condition and assumes that the wall layers are non-existent (and therefore that the free surface has uniform curvature throughout the cross-section), the flow rate becomes indeterminate, as will be seen shortly. To deal with these conflicting requirements, we have in this work decided to calculate the 'fully developed' instantaneous flow rates in a modified geometry where a small linear gradient is introduced in the channel height H, as shown in Figure 4. This idealization enables us to do away with the wall layers and impose a free surface that has everywhere, to leading order, a constant radius of curvature that does satisfy the contact angle requirement of (3). At the inlet and outlet of this modified device, the channel heights are

given by

$$H_{\mathrm{i}} = \frac{2H}{1+\delta}, \quad H_{\mathrm{o}} = \frac{2\delta H}{1+\delta} = \delta H_{\mathrm{i}} \tag{4}$$

Here δ is a parameter satisfying $0 < \delta \leqslant 1$ and is chosen as follows. Note that δ has been fixed so that the average channel height is H (which occurs at the middle section of the device because of the linear gradient). We obtain the radii of curvature of the free surface of the device of Figure 4 at the inlet and outlet from (3):

$$R_{\mathrm{i}} = \frac{H_{\mathrm{i}}}{2\cos\alpha}, \qquad R_{\mathrm{o}} = \frac{H_{\mathrm{o}}}{2\cos\alpha} \tag{5}$$

Assume that the curvature of the free surface in the flow direction (X) in the geometry of Figure 4 is negligibly small (i.e. the radii of curvature in the flow direction are much larger as compared to R_{i} and R_{o}); this assumption which will be justified in what follows. From (1), one may deduce the pressure difference between the inlet and the outlet of the device as:

$$P_1 - P_2 = \sigma\left[\frac{1}{R_{\mathrm{o}}} - \frac{1}{R_{\mathrm{i}}}\right] \tag{6}$$

Equating this result with the right hand side of (2) and upon using (4) and (5), a quadratic equation for δ is obtained, which is solved as follows:

$$\delta = \sqrt{T^2+1} - T, \quad T = \frac{H}{\cos\alpha}\left[\frac{1}{R_2} - \frac{1}{R_1}\right] \tag{7}$$

Note that δ does satisfy $0 < \delta \leqslant 1$ as required. Typically we expect $T \to 0$ and $\delta \to 1$, because H is very small as compared to the compartment meniscus radii R_1 and R_2.

Let us now pause and consider the rationale for the idealization done in going from the geometry of Figure 2 to that in Figure 4. This would be difficult to justify rigorously from a mathematical point of view. The expectation is that at least when $\delta \to 1$, this modification affects only the flow in the small layers near the wall, but without disturbing the contact angle; as we will see, the computed solution actually maintains the contact angle to higher order. Since the free surface in the bulk of the cross-section is unaffected and further, the contact angle is also maintained, one expects that the computed flow in the modified geometry of Figure 4 will be very close to that in Figure 2.

In summary, the problem now is to determine the flow rate at each instant in the idealized geometry of Figure 4; given the volumes of fluid at the inlet and outlet compartments, the meniscus radii R_1 and R_2 may be calculated; Equation (7) then gives δ. The instantaneous pressure drop, $P_1 - P_2$, is given by (2) and to leading order the free surface has uniform curvature at every cross-section, with the radius of curvature being calculated from the requirement that the contact angle be maintained. For example, Equation (5) determines the radii of the free surface at the inlet and outlet of the device, while (3) determines that at the middle section ($X = L/2$).

2.2. Idealization of the flow equations

We have already indicated in Section 2.1 that the flow is assumed to be quasi-steady; the instantaneous time dependence of the flow equations may be ignored. A 'slowly varying'

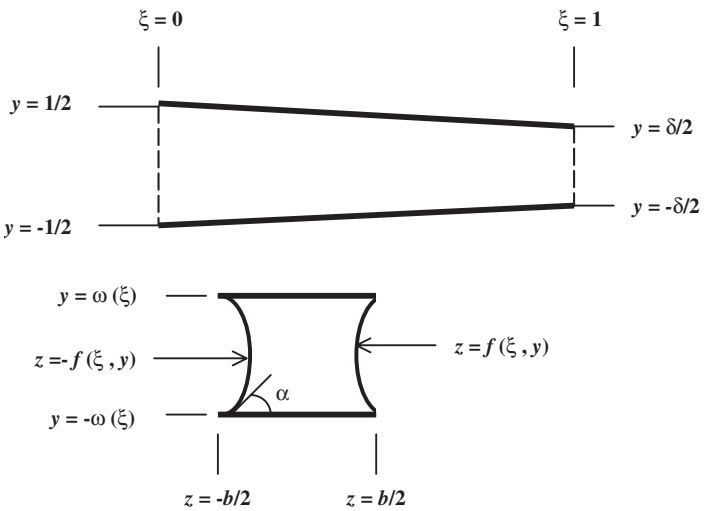

Figure 5. Non-dimensionalization of the geometry in Figure 4.

(with respect to time) pressure drop is being imposed on the device of Figure 4; δ starts with a value close to 1 and very slowly reaches the value of 1, when the pressures at the inlet and outlet of the PMD in Figure 1 get equalized. This assumption holds very well in practice because the inlet and outlet compartments have much larger cross-sectional areas as compared to that of the channel. Because the flow rates are extremely small, the temporal rates of change of the compartment levels and therefore of the meniscus radii and the corresponding fluid pressures are also extremely small. Secondly we assume that the length L of the device is large as compared to the channel height H and all quantities in the 'fully developed' region of Figure 2 (and hence Figure 4) are also 'slowly varying' in the flow direction, X. All lengths are non-dimensionalized with respect to H_i of (4) and we introduce the co-ordinate system (x, y, z) and a small parameter ε, where

$$x = X/H_i, \quad y = Y/H_i, \quad z = Z/H_i, \quad \varepsilon = H_i/L$$

All variables in the flow equations are assumed to be functions of εx in order to translate the above assumption into practice. The equations for the channel height and the (leading-order) free-surface shape in non-dimensional form are given by

$$\omega(\xi) \equiv \tfrac{1}{2}[(\delta - 1)\xi + 1], \quad (-\omega(\xi) \leqslant y \leqslant \omega(\xi), \ \xi \equiv \varepsilon x, \ 0 \leqslant \xi \leqslant 1) \tag{8}$$

$$-f(\xi, y) \leqslant z \leqslant f(\xi, y), \quad f(\xi, y) \equiv \frac{b}{2} + \omega(\xi)\tan\alpha - \sqrt{\frac{\omega^2(\xi)}{\cos^2\alpha} - y^2}, \quad b = \frac{B}{H_i} \tag{9}$$

Figure 5 illustrates the co-ordinate system and the geometry of Figure 4 in non-dimensional form. Equations (8) and (9) are in tune with the assumptions of Section 2.1, namely that a linear gradient in the channel height and a uniformly circular shape of the leading-order free surface (which maintains the contact angle at all x) are imposed. Now let the

velocities, pressure and surface tension coefficient be non-dimensionalized by V^*, P^* and σ^*, where

$$V^* = \frac{P^* H_i}{\mu}, \quad P^* = P_1 - P_2, \quad \sigma^* = H_i P^*$$

Here μ is the fluid viscosity and (2) and (4) define the other quantities. Now let (u, v, w) be the non-dimensional velocity components in the (x, y, z) co-ordinate directions and let p and λ be the non-dimensional pressure and surface tension coefficient ($\lambda = \sigma/\sigma^*$). Note that λ may be obtained from the following:

$$\lambda \equiv \frac{\sigma}{H_i(P_1 - P_2)} = \frac{\delta}{2(1-\delta)\cos\alpha} \tag{10}$$

The second equality follows from (4)–(6). The above non-dimensionalization yields a Reynolds number (R_e) given by

$$R_e = \frac{H_i^2 P^* \rho}{\mu^2}$$

The non-dimensional fluid pressure p may now be obtained from (1) as follows, upon neglecting the curvature of the free surface in the flow direction (which, from (9), may easily seen to be of higher order):

$$p(\xi, y, z) - p_0 = -\frac{\lambda \cos\alpha}{\omega(\xi)} + \hat{p}(\xi, y, z) \tag{11}$$

where $\hat{p}$ is a higher-order term satisfying

$$\hat{p}(\xi, y, z) = O(\varepsilon)$$

Here p_0 is the non-dimensional ambient pressure. Let us assume that R_e is sufficiently small such that

$$\varepsilon^2(1-\delta)R_e \ll 1$$

This enables us to neglect the inertial terms in the perturbed flow equations. Assuming that the component velocities (u, v, w) are each functions of (ξ, y, z) and upon neglecting all higher-order terms (in particular, the time derivatives, the inertial terms and all second derivatives with respect to x) in the Navier–Stokes equations, the following governing equations are obtained to leading order:

$$\Delta u = -\frac{\varepsilon(1-\delta)\lambda\cos\alpha}{2\omega^2(\xi)}, \quad \Delta v = p_y, \quad \Delta w = p_z \tag{12}$$

where

$$\Delta \equiv \frac{\partial^2}{\partial y^2} + \frac{\partial^2}{\partial z^2}$$

and the continuity equation is given by

$$u_x + v_y + w_z = 0 \tag{13}$$

Here the subscripts denote partial derivatives. We will look for solutions to (12) and (13) in which u is symmetric about the planes $y=0$ and $z=0$ and v and w satisfy the corresponding obvious symmetry conditions in y and z as indicated, for example, by (13). We may therefore confine our attention to the domain in which y and z are non-negative. These symmetry conditions are specified by

$$u_y = v = w_y = 0 \quad \text{at } y=0 \quad \text{and} \quad u_z = v_z = w = 0 \quad \text{at } z=0 \tag{14}$$

At the solid wall $y=\omega$, the no-slip and no-normal velocity boundary conditions must be satisfied:

$$(u,v,w) = (0,0,0) \quad \text{at } y=\omega(\xi), \quad z\in[0,b/2], \quad \xi\in[0,1] \tag{15}$$

At the free surface, the kinematic boundary condition is that the normal component of the vector velocity $\mathbf{u}[=(u,v,w)]$ must vanish. This may be stated to leading order as follows:

$$\mathbf{u}\cdot\nabla(f(\xi,y)-z) \equiv \varepsilon u f_\xi + v f_y - w = 0 \text{ at } z=f(\xi,y), \quad (y\in[0,\omega(\xi)] \text{ and } \xi\in[0,1]) \tag{16}$$

Here ∇ is the gradient vector $(\partial/\partial x, \partial/\partial y, \partial/\partial z)$. In the ensuing section, it will be seen that the terms $\varepsilon u, v$ and w in the above equation are all $O(\varepsilon^2)$; in particular, the assumption that the flow is 'locally parallel' cannot be made here because the contribution from the term proportional to u is, in general, not negligible. The dynamic boundary condition at the free surface is that the stress be continuous across the interface, except for surface tension effects. The normal component of the stress at the free surface, which is the sum of the pressure and the dynamic stress terms, must therefore satisfy the dynamic equivalent of the Laplace–Young equation (which has already been imposed to leading order in (11)). Since the gas phase does not support shear stresses, the tangential component of the stress at the free surface must vanish; this condition may be stated as:

$$\tau_t = 0 \quad \text{at the free surface} \tag{17}$$

where τ_t is the tangential component of the stress.

Finally, note that the perturbation pressure $\hat{p}$ (where $\hat{p}$ represents the $O(\varepsilon)$ component of the pressure indicated in (11)) will induce a higher-order perturbation to the free surface that will, in general, be of non-uniform curvature. The condition that the perturbed free surface maintain the contact angle along the contact line $(y,z)=(\omega,b/2)$ is also required to hold. This condition, not stated here, is somewhat complicated because of the fact that the leading-order free surface also exhibits an $O(\varepsilon(1-\delta))$ deviation from the actual physical contact angle, which is a three-dimensional entity (defined as the angle between the normal to the free surface and the normal to the solid boundary at the contact line).

3. SOLUTION PROCEDURE

In this section the solution procedure will be outlined, skipping the obvious algebraic details. In Section 4, qualitative justification is provided for the steps in this procedure.

Define

$$\phi_n(\xi) \equiv \frac{(2n-1)\pi}{2\omega(\xi)}, \quad n = 1, 2, \ldots \quad \text{and} \quad \kappa_m = \frac{2m\pi}{b}, \quad m = 0, 1, 2, \ldots \tag{18}$$

In what follows the functional dependencies of various quantities (for example on ξ) will be assumed to be understood when not indicated. A solution $\mathbf{u}$ to (12) and (13) that satisfies (14) is assumed as follows:

$$\mathbf{u} = (u_3, v_3, w_3) + (0, v_2, w_2) \tag{19}$$

where the two velocity vectors on the right hand side each satisfy (12) and (13) (but not necessarily (14)) and are three-dimensional (3-D) and planar, respectively. The planar velocity $(0, v_2, w_2)$ has a parametric dependence on ξ and can be expressed in terms of a stream function that satisfies the biharmonic equation in the y–z plane.

3.1. The three-dimensional solution

First the 3-D solution, which is obviously critical for the flow rate calculation, will be described. The most general solution for u that satisfies (12), (14) and (15) is given by

$$u_3 = \frac{(1-\delta)\varepsilon(\omega^2 - y^2)\lambda\cos\alpha}{4\omega^2} + \varepsilon\sum_{n=1}^{\infty} A_n(\xi)\cos(\phi_n y)\cosh(\phi_n z) \tag{20}$$

where A_n represent arbitrary functions; determination of these will yield the flow rate. Note that each term of the series in (20) is a harmonic (in y and z) eigenfunction; the quadratic term satisfies (12). The functional form for w_3 is assumed as a double Fourier series, as follows:

$$w_3 = \varepsilon^2 \sum_{m=1}^{\infty}\sum_{n=1}^{\infty} C_{mn}(\xi)\,\cos(\phi_m y)\sin(\kappa_n z) \tag{21}$$

where C_{mn} are functions to be determined. Upon substituting the above into the continuity equation (13) and integrating, we obtain the following equation for v_3, with primes indicating differentiation with respect to ξ:

$$\begin{aligned} v_3 = {} & \frac{(1-\delta)^2\varepsilon^2 y^3\lambda\cos\alpha}{12\omega^3} + \varepsilon^2\sum_{n=0}^{\infty} B_n(\xi)\cos(\kappa_n z) - \frac{2\varepsilon^2\omega}{\pi}\sum_{n=1}^{\infty}\frac{A_n'}{(2n-1)}\sin(\phi_n y)\cosh(\phi_n z) \\ & + \frac{\varepsilon^2(1-\delta)}{2\omega}\sum_{n=1}^{\infty} A_n[\{\varphi_n^{-1}\sin(\phi_n y) - y\cos(\phi_n y)\}\cosh(\phi_n z) - z\sin(\phi_n y)\sinh(\phi_n z)] \\ & - \frac{4\omega}{b}\varepsilon^2\sum_{m=1}^{\infty}\sum_{n=1}^{\infty}\left(\frac{n}{2m-1}\right) C_{mn}\sin(\phi_m y)\cos(\kappa_n z) \end{aligned} \tag{22}$$

where B_n are arbitrary functions, to be determined. It is extremely important to note that requiring v_3 to satisfy (14) would force $B_n \equiv 0$ for all n. This is not done here for reasons that will be clear later on; the asymmetry introduced will be taken care of by a corresponding

asymmetry in v_2. We now substitute (21) and (22) into (12) and obtain suitable expressions for p_y and p_z, noting that the terms proportional to A_n and A'_n in (22) are harmonic. Upon requiring $p_{yz} = p_{zy}$, one finds that the z-dependence of this equation is identically satisfied; the y-dependence may be shown to hold upon using orthogonality, i.e. multiplying by $\sin(\phi_j y), j = 1, 2, \ldots$, and integrating on $y \in [0, \omega]$. This procedure results in C_{mn} being determined as follows:

$$C_{mn}(\xi) = D_{mn}(\xi) B_n(\xi), \quad m = 1, 2, \ldots, \quad n = 1, 2, \ldots \tag{23}$$

where D_{mn} is defined by

$$D_{mn}(\xi) \equiv \frac{32 n^3 \pi^2}{(2m-1) b^3 [\phi_m^2(\xi) + \kappa_n^2][\phi_m(\xi) + (8\omega(\xi) n^2 \pi)/((2m-1)b^2)]}$$

Having satisfied the continuity and momentum equations, we now turn our attention to the boundary conditions. The no-normal velocity condition (15) will now be imposed on v_3. Insert (23) into (22), set $y = \omega$ and require $v_3 = 0$; multiplying the resulting equation by $\cos \kappa_j z$, $j = 0, 1, 2, \ldots$ and integrating on $z \in [0, b/2]$ (using orthogonality), the following expressions are obtained for B_j:

$$B_0(\xi) = -\frac{(1-\delta)^2 \lambda \cos\alpha}{12} + \frac{8\omega^2(\xi)}{b\pi^2} \sum_{n=1}^{\infty} \frac{(-1)^{n+1} A'_n(\xi)}{(2n-1)^2} \sinh\left[\frac{\phi_n(\xi) b}{2}\right]$$
$$- \frac{(1-\delta)}{b\pi} \sum_{n=1}^{\infty} \frac{(-1)^{n+1} A_n(\xi)}{(2n-1)} \left\{ \frac{4}{\phi_n(\xi)} \sinh\left[\frac{\phi_n(\xi) b}{2}\right] - b \cosh\left[\frac{\phi_n(\xi) b}{2}\right] \right\} \tag{24}$$

and for $j \geqslant 1$,

$$B_j(\xi) = \frac{8\omega(\xi)}{b\pi} \sum_{n=1}^{\infty} \left[\frac{(-1)^{n+1} J_{nj}(\xi) A'_n(\xi)}{2n-1} \right] + \frac{2(1-\delta)}{b\omega(\xi)} \sum_{n=1}^{\infty} (-1)^n A_n(\xi) \left[\frac{J_{nj}(\xi)}{\phi_n(\xi)} - I_{nj}(\xi) \right] \tag{25}$$

where

$$J_{nj}(\xi) = \frac{(-1)^j 2\omega(\xi)(2n-1) b^2 \sinh[(\phi_n(\xi) b)/2]}{\pi H_j(\xi)[(2n-1)^2 b^2 + 16\omega^2(\xi) j^2]}$$

$$I_{nj}(\xi) = \left[\frac{16\omega^2(\xi) j^2}{\{16\omega^2(\xi) j^2 + (2n-1)^2 b^2\} H_j(\xi)} \right]$$
$$\times \left[\frac{(-1)^j (2n-1) b^3}{16\omega(\xi) j^2 \pi} \cosh\left\{ \frac{\phi_n(\xi) b}{2} \right\} + \left\{ \frac{1}{\phi_n(\xi)} - \frac{(2n-1) b^2}{8\omega(\xi) j^2 \pi} \right\} J_{nj}(\xi) \right]$$

and H_j is defined by

$$H_j(\xi) = 1 + \frac{4\omega(\xi) j}{b} \sum_{m=1}^{\infty} \frac{(-1)^m D_{mj}(\xi)}{2m-1}$$

One may now express w_3 and v_3 in (21)–(22) in terms of only A_n (and its derivative) as the unknown functions. In order to determine these, if we now implement the free surface boundary condition (16), a vector first order ordinary differential equation would be obtained, in which the independent variable is ξ and the dependent variable is the vector $[A_1(\xi), A_2(\xi), \ldots, A_N(\xi)]$ (where the number of unknowns is truncated at N). The solution to this differential equation may be uniquely determined only if an additional constraint is specified. The relevant condition is that the flow rate in the device be a constant, independent of ξ:

$$\Theta(\xi) = \varepsilon\Gamma = \text{constant for all } \xi \in [0,1] \quad \text{where } \Theta(\xi) \equiv 4\int_0^{\omega(\xi)} \int_0^{f(\xi,y)} u_3(\xi, y, z)\, \mathrm{d}z\, \mathrm{d}y \tag{26}$$

Note that it cannot be taken for granted that (26) will be automatically satisfied even if it is not imposed, because the 3-D solution fails to satisfy the symmetry constraint $v_3 = 0$ at $y = 0$. The free surface boundary condition (16), when implemented for the 3-D component $\mathbf{u} = (u_3, v_3, w_3)$, may be stated as follows (upon using (23)–(25) to eliminate C_{mn} and B_n from (21)–(22)):

$$\sum_{n=1}^{\infty} [P_n(\xi, y) A_n'(\xi) + Q_n(\xi, y) A_n(\xi)] = R(\xi, y) \tag{27}$$

Here the expressions for P_n, Q_n and R are given in Appendix A. Upon substituting for u_3, (26) reduces to

$$\sum_{n=1}^{\infty} [\Phi_n(\xi) A_n(\xi)] - \Gamma = -\Gamma_Q(\xi) \tag{28}$$

where

$$\Phi_n(\xi) = \frac{4}{\phi_n(\xi)} \int_0^{\omega(\xi)} \cos[y\phi_n(\xi)] \sinh[f(\xi, y)\phi_n(\xi)]\, \mathrm{d}y$$

and

$$\Gamma_Q(\xi) = (1-\delta)\lambda\omega^2(\xi) \left[\frac{2\sin\alpha}{3} - \frac{1}{4\cos\alpha} \left\{ \frac{(\pi - 2\alpha)(1 + 2\cos 2\alpha)}{2(1 + \cos 2\alpha)} + \frac{\tan\alpha}{2}(2 + \cos 2\alpha) \right\} \right] + [b\omega(\xi)(1-\delta)\lambda\cos\alpha]/3 \tag{29}$$

Equations (27) and (28) are critically important in our solution scheme in the sense that their satisfaction guarantees the existence of the planar solution; this issue will be discussed further in Section 4. The problem now is to solve (27) and (28) for the unknown functions $A_n(\xi)$ and the constant Γ (which determines the flow rate as specified in (26)). The numerical algorithm that accomplishes this solution is described in Section 6. The 3-D component of the term $\hat{p}$ in (11) may now be stated as

$$\hat{p}_3(\xi, y, z) = \frac{\varepsilon^2(1-\delta)^2[y^2 - \omega^2(\xi)]\lambda\cos\alpha}{4\omega^3(\xi)} + \frac{\varepsilon^2 b}{2\pi} \sum_{m=1}^{\infty} \sum_{n=1}^{\infty} \frac{C_{mn}(\xi)}{n} [\phi_m^2(\xi) + \kappa_n^2] \cos[\phi_m(\xi) y] \cos(\kappa_n z) \tag{30}$$

where C_{mn} is specified by (23) and (25). After simplifications, we obtain the following expression for $\partial \hat{p}_3/\partial y$ along the contact line:

$$\partial \hat{p}_3/\partial y = 4\omega(\xi)\varepsilon^2 \Re(\xi)/b \quad \text{at } (y,z) = (\omega, b/2)$$

where

$$\Re(\xi) = \sum_{n=1}^{\infty} [F_n(\xi) A_n'(\xi) + G_n(\xi) A_n(\xi)] - S(\xi) \tag{31}$$

Here F_n, G_n and S are defined by

$$F_n(\xi) = \frac{8\omega(\xi)}{b\pi(2n-1)} \sum_{j=1}^{\infty} \frac{(-1)^{j+n+1}}{j} E_j(\xi)\, J_{nj}(\xi)$$

$$G_n(\xi) = \frac{2(1-\delta)}{b\omega(\xi)} \sum_{j=1}^{\infty} \frac{(-1)^{j+n}}{j} E_j(\xi) \left[\frac{J_{nj}(\xi)}{\phi_n(\xi)} - I_{nj}(\xi) \right]$$

$$S(\xi) = -\frac{2(1-\delta)^2 \lambda \cos\alpha}{b\omega(\xi)}$$

and E_j is given by

$$E_j(\xi) = \sum_{m=1}^{\infty} (-1)^m (2m-1) D_{mj}(\xi) [\phi_m^2(\xi) + \kappa_j^2]$$

As will be described in Section 6, a weighted least-squares algorithm is used to implement (27) and (28). We have included in the least-squares procedure the requirement $\Re(\xi) = 0$ in (31), with an extremely small weightage. The idea is that the deviations from $\Re(\xi) = 0$ should be kept at manageable levels but without compromising on (27) and (28); if this condition is not imposed, the flow rate is not significantly affected, but the stresses at $y = \omega$, especially near the contact line, become large. If the weightage given to $\Re(\xi) = 0$ is sufficiently small, the performance of the algorithm with respect to (27) and (28) improves.

In general, the 3-D solution will exhibit deviations from (17) that are $O(\varepsilon)$; this is so because the tangential stresses at the free surface would contain terms proportional to the gradient of u_3 in the y and z directions, which are assumed to be $O(\varepsilon)$ everywhere (except possibly at the contact line). Neglect of the boundary condition (17) to leading order is justified by the fact the normal stress at the free surface, (namely, the pressure to leading order), is $O(1/(1-\delta))$, as is evident from (10) and (11); this dominates the tangential component, which is $O(\varepsilon)$. Equation (17) may be taken care of at the next level of approximation, when the free surface is perturbed; we will not go into this issue here because it is not relevant to the computation of the leading-order flow rate.

3.2. The planar solution

For the planar solution to exist, the net (two-dimensional) flow into every cross-section must vanish. If (27) and (28) are satisfied by the 3-D solution (and this is assumed to be the case), our goal in this section is to show that the boundary conditions for the planar solution will be compatibile with this requirement. Denote by $\psi(y,z;\xi)$ the stream function for the planar

solution, with

$$w_2 = \psi_y \quad \text{and} \quad v_2 = -\psi_z$$

Then ψ satisfies the biharmonic equation:

$$\Delta\varpi = 0, \quad \text{where} \quad \varpi = -\Delta\psi \tag{32}$$

Here ϖ is the vorticity of the planar solution. The following boundary conditions are imposed on the planar solution:

$$\begin{aligned}
&y = \omega(\xi): && \psi = \psi_y = 0 \\
&z = 0: && \psi = \varpi = 0 \\
&y = 0: && \psi = \varepsilon^2 z B_0(\xi) + \varepsilon^2 \sum_{j=1}^{\infty} \frac{B_j(\xi)\sin\kappa_j z}{\kappa_j}, \quad \varpi = \varepsilon^2 \sum_{j=1}^{\infty} \kappa_j B_j(\xi)\sin\kappa_j z \\
&z = f(\xi, y): && \psi = 0
\end{aligned} \tag{33}$$

At $y = 0$, the stated boundary conditions represent the requirements that the deviation in v_3 be cancelled and that $\partial w_2/\partial y$ vanish. At the free surface $z = f$, the normal velocity component of the 2-D solution must vanish and hence we have required $\psi = 0$. The other (unstated) higher-order boundary conditions at the free surface are that the deviation from (17) vanish and that the dynamic equivalent of the Laplace–Young equation be satisfied. Here three-dimensional effects must be accounted for in order to arrive at the higher-order terms in the normal stress balance. Both of these conditions cannot be imposed while retaining the assumed free surface; the actual free surface must be determined iteratively by perturbing it by $O(\varepsilon)$ (while maintaining the contact angle to higher-order) such that the above boundary conditions are satisfied.

It is clear that if the planar solution exists, then the full solution will indeed satisfy all the boundary conditions. A crucial requirement for the existence of ψ is apparent from (33). Denote

$$f_0(\xi) = f(\xi, 0), \quad \psi_0(\xi) = \psi(0, f_0; \xi)$$

To avoid a discontinuity in ψ at the corner point $(y,z) = (0, f_0(\xi))$ (and therefore to ensure that the planar solution exists) it is essential that $\psi_0(\xi)$ vanish identically for all ξ. From (33), it is clear that this requirement reduces to

$$\psi_0(\xi)/\varepsilon^2 = f_0(\xi)B_0(\xi) + \sum_{j=1}^{\infty} \frac{B_j(\xi)\sin[\kappa_j f_0(\xi)]}{\kappa_j} = 0 = \frac{1}{\varepsilon^2}\int_0^{f_0} v_3(\xi, 0, z)\,\mathrm{d}z \tag{34}$$

It is easy to show that (34) will be true provided the 3-D solution satisfies (27) and (28); this follows from an elementary mass balance on a segment of the channel of length dx in Figure 4. It is very important to note that, in general, the planar solution will not exist if the 3-D solution fails to satisfy (27) and/or (28). For example, if (27) is false (but (28) is true) then the free surface condition in (33) must be modified in order to ensure that the *three-dimensional* contribution to the normal velocity from (27) is cancelled out. But then there is no guarantee that the two-dimensional mass balance will be satisfied. Note that prescribed normal velocities are being imposed across all four walls of the cross-section, and they need

not be compatible; in general, one would end up with an unacceptable discontinuity in ψ at one of the corner points of the cross-section. This argument explains why we have required (27) and (28).

We will not describe the numerical algorithm for the planar solution, which is well known, and does not affect the leading-order flow rate. We may now proceed with the perturbation solution by considering the $O(\varepsilon)$ pressure term, which will induce an $O(\varepsilon^2)$ component in u via its pressure gradient and $O(\varepsilon^3)$ terms in v and w via continuity, etc.

4. JUSTIFICATION FOR SOLUTION PROCEDURE

The planar velocity components v_2 and w_2, which are uniformly $O(\varepsilon^2(1-\delta))$ everywhere, must become rapidly varying in y and z in a layer near the free surface so that the induced pressure gradients and tangential stresses at the free surface become $O(\varepsilon)$ and match the required boundary conditions. We may arrive at the conclusion that there is significant viscous dissipation due to rapid variations in y and z in the planar solution near the free surface. This dissipation will significantly reduce the flow rate obtainable for the given average pressure gradient. Numerical solutions reported in Sections 7 and 8 support this conclusion.

One could still ask whether requiring the 3-D solution to satisfy (27) and (28) is the *only* way to ensure that the planar solution exists. This appears extremely likely to the author; note that an alternative method, if it exists, must work at *every location* in ξ. However, there are other possible solutions than the one proposed here which we will discuss below. Consider the following modification of (21):

$$w_3 = \varepsilon^2 \sum_{m=1}^{\infty}\sum_{n=1}^{\infty} C_{mn}(\xi)\cos(\phi_m y)\sin(\kappa_n z) + \varepsilon^2 \sum_{m=1}^{\infty} \Xi_m(\xi)\cos(\phi_m y)\sinh(\phi_m z) \tag{35}$$

where $\Xi_m(\xi)$ are arbitrary functions. The additional terms in (35) represent harmonic (in y and z) eigenfunctions that will induce a corresponding change in v_3 (Equation (22)) via the continuity equation. Equation (23) still holds, but (24) and (25) would have to be suitably modified. The point is that we now have extra degrees of freedom available to satisfy (27) and (28). It appears that the functions $\Xi_m(\xi)$ can be fixed arbitrarily and different choices will, in general, lead to different coefficients $A_n(\xi)$ and hence different flow rates. Here it is important to recognize that the double Fourier series in (21), which vanishes on the closed boundary $y = \pm\,\omega,\ z = \pm\, b/2$, does not contain within it any harmonic terms. The only solution of Laplace's equation that so vanishes is zero. The justification for setting $\Xi_m = 0$ is that in the postulated 'fully developed' zone, cross flow in the z-direction ought to be minimal. The harmonic terms in (35), which would induce corresponding harmonic terms in v_3 (via continuity) and u_3 (via the induced change in the coefficients A_n), represent such cross flow. We expect that the cross flow represented by the double Fourier series is the minimum possible and would be substantially cancelled near $y = 0$ when symmetry is forced via the planar solution (see ensuing paragraph).

Let us now consider an alternative solution procedure that may at first sight look easier and more logical. Let w_3 be chosen as in (35). Suppose the symmetry requirement were to be imposed on v_3 and therefore $B_j \equiv 0$ in (22). Then by (23) we need $C_{mn} \equiv 0$ and hence w_3 will consist only of the harmonic terms. One consequence is that now v_3 (obtained from continuity as before) will not satisfy the no-normal velocity condition at $y = \omega$. The question is whether

Ξ_m and A_n can be chosen to satisfy this condition in addition to suitably modified versions of (27) and (28). The catch here is that this 3-D solution is not the most general possible because the z-component w_3 has been restricted to be harmonic. We have confirmed that this solution procedure fails for the special case in which $\Xi_m = 0$ and the no-normal velocity condition at $y = \omega$ is ignored (this can always be taken care of by the planar solution). When one attempts to satisfy (16), the coefficients A_n rapidly diverge with increasing n, making the resulting velocities very large and oscillatory. In summary, it appears that a non-harmonic w_3 as postulated by the double Fourier series in (21) is necessary in order to be able to implement (16) and determine $A_n(\xi)$.

We next use energy considerations to derive an upper bound for the flow rate. Consider the geometry of Figure 2 in which the channel width is B, the height is H (with no gradient imposed) and with the instantaneous pressure difference over the length L being given by (2). Assume further that the 'free surface' is in fact a solid boundary with slip allowed (but no normal velocity) and which has the shape of a circular arc that maintains the contact angle. If one now calculates δ as in (7) and uses the same non-dimensionalization as before, the 'fully developed' velocity profile in this device would be

$$u = (1 - \delta)\varepsilon \left[\frac{1}{4} - y^2\right] \lambda \cos\alpha, \quad v \equiv 0, \quad w \equiv 0$$

The solution for u is obtained from (20) by setting $A_n \equiv 0$ and $\omega = 0.5$. We claim that the flow rate in this hypothetical device, given by $\varepsilon\Gamma_Q(0.5)$ (see (29)), is an upper bound for the flow rate in the 'actual' device of Figure 4, computed by the prescribed solution procedure. The reason for this claim is that the actual device has the same (leading-order) pressure gradient and length as the hypothetical one, but also has cross-flow dissipation due to non-zero v and w. Therefore a significant portion of the energy supplied to maintain the pressure gradient is dissipated in sending the fluid along a spiraling path from inlet to outlet, as compared to the straight path in the hypothetical device. This dissipation due to cross flow is not negligible, as explained earlier. Further, for a given contact angle, the ratio of the actual flow rate to this upper bound of $\varepsilon\Gamma_Q(0.5)$ must decrease with increasing aspect ratio B/H, because cross-flow effects can be expected to increase as aspect ratio increases (over a reasonable range of values). It is heartening that the computed solution satisfies these two important checks (in addition to others), as shown in Sections 7 and 8. Note also that the computed flow rate must be the maximum possible for the given pressure gradient, given that the cross flow effects have been minimized.

Finally, an important question that arises is how small should the parameters ε and $(1 - \delta)$ be in order for valid results to be obtained. One way to estimate this *a posteriori* is to check whether the perturbation pressure $\hat{p}$ is sufficiently smaller than the leading term in (11). Since λ as defined in (10) is $O(1/[1 - \delta])$, the criterion for validity of our results may be stated as:

$$|(1 - \delta)\hat{p}(\xi, y, z)| \ll 1 \tag{36}$$

This equation must hold throughout the domain, but is particularly important at $z = f$; otherwise the assumed circular shape of the leading-order free surface would be in error. Note that $\hat{p}$ in (36) is given by

$$\hat{p}(\xi, y, z) = \hat{p}_2(\xi, y, z) + \hat{p}_3(\xi, y, z)$$

where $\hat{p}_2(=O(\varepsilon))$ is the contribution to the pressure from the planar solution and $\hat{p}_3$ is given by (30). Equation (36) can be checked *a posteriori*, after the coefficients A_n have been calculated for a given δ and after the planar solution has been computed.

5. ADVANTAGES OF PRESENT APPROACH

Before presenting the numerical algorithm in the ensuing section, we pause to consider the significant advantages gained with our semi-analytical approach. First consider a very important invariance property of Equations (27) and (28). Multiply (28) by $(1-\delta)$ and consider the δ-dependent terms in (27) and (28). Observe that on the left hand side of these equations, the terms A_n are multiplied by $(1-\delta)$; on the right hand side appears the term $(1-\delta)^2\lambda$, which, from (10), is proportional to $\delta(1-\delta)$; the ξ-dependence of every function in these equations occurs only through $\omega(\xi)$, which, via (8), is actually a function of $(1-\delta)\xi$ with no other δ-dependent terms. These observations indicate the following transformations:

$$\hat{\xi}=(1-\delta)\xi, \quad \omega(\xi)=\hat{\omega}(\hat{\xi}), \quad A_n(\xi)=\delta\hat{A}_n(\hat{\xi}), \quad \Gamma=\delta\hat{\Gamma}, \quad A_n'(\xi)=\delta(1-\delta)\hat{A}_n'(\hat{\xi}) \tag{37}$$

Every other function of ξ in (27) and (28) now becomes a 'hatted' function of $\hat{\xi}$ with no explicit δ-dependence. It is easy to see that all explicit δ-dependent terms drop out of the transformed equations; the *only* δ-dependence of these 'hatted' equations is via the fact that the range of the independent variable $\hat{\xi}$ is now on $\hat{\xi}\in[0,(1-\delta)]$. One concludes that once these transformed equations (and hence (27) and (28)) have been solved for one particular value of δ, say the initial (in time) value $\delta=\delta_0$, they have in fact been solved for *all* δ in the semi-open interval $[\delta_0,1)$. This argument applies to $\Re=0$ in (31) as well, which is included (with a very small weightage) in our algorithm. In other words, the time dependence has been effectively removed from the problem. Nevertheless it is convenient to push through the numerical solution of the equations in the stated form (with ξ as the independent variable), subject to another transformation described in the ensuing section.

The advantages gained with our approach can now be clearly appreciated. As we have just seen, if one successfully solves for the flow rate at the initial instant, one has solved for all of these. Secondly one only needs to discretize the first order derivatives of $A_n(\xi)$; since these are actually functions of $\hat{\xi}$, they are 'slowly varying' provided $\delta\to 1$, as is usually the case. Therefore only a relatively crude grid in ξ is needed in order to obtain the desired accuracy. Further, one may use a higher-order accurate finite difference scheme without running into numerical instability. Note that the 'fast variations' in y and z (especially near the free surface) have been taken care of analytically. Because the shape of the free surface is known to leading order, no iterative procedures are needed. And because we are dealing with exact solutions of the governing equations, we need only worry about the accuracy to which the boundary conditions are satisfied, in order to be reasonably certain that the small flow rates are accurately computed.

Contrast this with the direct numerical simulation approach. A full-fledged three-dimensional time-dependent simulation in a complex geometry and to a very demanding accuracy (because of the small flow rates, of the order of 10^{-4} in non-dimensional terms) must be carried out. The entry and exit regions cannot be ignored, because otherwise we do not know the boundary conditions to be imposed. The flow parameters are rapidly varying in all three directions at the

entry/exit regions because of the rapid changes in the geometry; elsewhere the rapid variation is still present in the y- and z-directions. Therefore the three-dimensional grid must be very fine near these regions; in view of the accuracy demand, the fine spatial discretizations needed would make the computation extremely costly in terms of both time and memory. Further, the time discretization must also be fine in view of the well-known stability limitations of such algorithms (via the 'CFL' criterion); for this reason, a higher-order spatially accurate scheme would make the computation costly in time as well. The cost factor is compounded by the fact that the free surface must be determined iteratively. Even if these formidable obstacles are overcome, one still cannot be sure of the accuracy of the computed flow except via prohibitively expensive grid refinement studies.

In short, a full-fledged three-dimensional numerical simulation is fraught with difficulties and requires highly sophisticated numerical techniques implemented on a genuine super-computer. The author, at least, is not aware of any instance in which such simulation results have been reported in the open literature. When one considers that with the present method, the total drainage time can be estimated in a single simulation (or maybe a few simulations, to optimize the numerical parameters) of a few seconds implemented on a personal computer with negligible memory requirements, the advantages should be obvious.

6. THE NUMERICAL ALGORITHM

The goal of this section is to describe the numerical algorithm in sufficient detail so as to enable interested readers to implement it. We first make a change of the dependent variables from A_n to $\tilde{A}_n$ as follows:

$$A_n(\xi) = \tilde{A}_n(\xi)\ \exp[-\phi_n(\xi)b/2] \tag{38}$$

Upon differentiating with respect to ξ, we obtain

$$A_n' = \exp[-\phi_n b/2]\left[\tilde{A}_n' + \left\{\frac{(2n-1)\pi b(\delta-1)}{8\omega^2}\right\}\tilde{A}_n\right]$$

The purpose of this important transformation is to ensure that the coefficients of the matrix (in the system of linear equations to be solved) are all bounded as $n \to \infty$; this makes the matrix relatively better conditioned. Secondly, the finite difference discretization errors in $\tilde{A}_n'$ get scaled down by the exponential factor in the above equation and therefore translate into much smaller errors in A_n'. These two factors make this transformation indispensable. Upon substituting (38) into (27), (28) and $\mathfrak{R} = 0$ in (31), we obtain

$$\sum_{n=1}^{\infty}[\tilde{P}_n(\xi, y)\tilde{A}_n'(\xi) + \tilde{Q}_n(\xi, y)\tilde{A}_n(\xi)] = R(\xi, y)$$

$$\sum_{n=1}^{\infty}[\tilde{\Phi}_n(\xi)\tilde{A}_n(\xi)] - \Gamma = -\Gamma_Q(\xi)$$

$$\sum_{n=1}^{\infty}[\tilde{F}_n(\xi)\tilde{A}_n'(\xi) + \tilde{G}_n(\xi)\tilde{A}_n(\xi)] = S(\xi)$$

where

$$(\tilde{P}_n, \tilde{\Phi}_n, \tilde{F}_n) = \exp[-\phi_n b/2](P_n, \Phi_n, F_n)$$

$$(\tilde{Q}_n, \tilde{G}_n) = \exp[-\phi_n b/2](Q_n, G_n) + \left\{ \frac{(2n-1)\pi b(\delta - 1)}{8\omega^2} \right\} (\tilde{P}_n, \tilde{F}_n)$$

In what follows, we will drop the tildes and describe the algorithm with respect to (27), (28) and (31). We take it as understood that the transformed equations, to which the algorithm equally applies, are actually being solved in practice. The interval $\xi \in [0,1]$ is discretized into I equally spaced points (ξ_i, $i = 1,2,\ldots,I$), where $\xi_1 = 0$ and $I \geqslant 5$. The grid spacing is given by $h = 1/(I-1)$. A fourth-order accurate finite difference scheme, using five-point interpolation, is used on this grid to discretize the derivatives $A_n'(\xi)$. The details of this scheme are given in Appendix B. Use the notation $\omega^i = \omega(\xi_i)$ and similarly for other functions. For all ω^i, discretize $y \in [0, \omega^i]$ into M uniformly spaced points (in increasing order) y^{il}, where $l = 1,2,\ldots,M$; denote by superscript il all functional dependencies on y^{il}. Let the number of harmonic eigenfunctions in (20) be truncated at N. Finally, let the number of terms in the j- and k-summations (which occur in the definitions of P_n, Q_n, F_n and G_n; see also Appendix A) be truncated at J and K respectively. This corresponds to taking J and K terms in the n- and m-summations respectively in the double Fourier series of (21); for a given N, these must be suitably high, for example, to ensure that the no-normal velocity condition at the solid wall is satisfied to required accuracy. Note that there are $IN + 1$ unknown constants A_n^i and Γ to be determined.

We have used a weighted least-squares algorithm to implement (27), (28) and (31). This algorithm is simple to describe: form the weighted sum $\bar{S}$ of the squares of the errors in (27), (28) and (31) with weight factors θ_1, θ_2 and θ_3 respectively; the summation is done over I points in each of (28) and (31) and IM points in (27). The requirement that that $\bar{S}$ be minimized yields the criterion that the partial derivative of $\bar{S}$ with respect to each of the $IN+1$ unknown constants A_n^i and Γ must vanish (treating these unknowns as the only minimization variables); these provide the $IN + 1$ equations for the unknowns. The least-squares approach has been around for several decades and has been used successfully in recent times by Shankar [14, 15] to solve biharmonic and Stokes flow problems in two and three dimensions. Define

$$\Psi_{jn}^{il} \equiv \frac{\partial}{\partial A_n^j}[P_n^{il} A_n'^i + Q_n^{il} A_n^i]$$

and

$$\mathfrak{I}_{jn}^{i} \equiv \frac{\partial}{\partial A_n^j}[F_n^{i} A_n'^i + G_n^{i} A_n^i]$$

Here the partial derivatives are interpreted in the usual way, treating the $IN + 1$ unknowns A_n^i and Γ as the variables. The formulae for the above quantities are omitted here; these are obtained in a completely straightforward manner upon discretizing the derivative terms as outlined in Appendix B. Further, define

$$\tau(i) = 1, \qquad i \leqslant 5$$
$$= i - 4, \quad i > 5$$

The least-squares algorithm for the discretization of Appendix B is as follows:

$$\sum_{i=1}^{I}\sum_{n=1}^{N}\left[\sum_{l=1}^{M}\left\{\theta_1\Psi_{jm}^{il}\sum_{k=\tau(i)}^{\tau(i)+4}\Psi_{kn}^{il}A_n^k\right\}+\theta_3\mathfrak{I}_{jm}^{i}\sum_{k=\tau(i)}^{\tau(i)+4}\mathfrak{I}_{kn}^{i}A_n^k\right]+\theta_2\Phi_m^j\left[\sum_{n=1}^{\infty}(\Phi_n^jA_n^j)-\Gamma\right]$$
$$=\sum_{i=1}^{I}\left[\theta_3\mathfrak{I}_{jm}^{i}S^i+\theta_1\sum_{l=1}^{M}\Psi_{jm}^{il}R^{il}\right]-\theta_2\Phi_m^j\Gamma_Q^j \tag{39}$$

for $j=1,2,\ldots,I$ and $m=1,2,\ldots,N$. Equations (39) and (28) (evaluated at $\xi=0$ and multiplied by the weight factor θ_2) provide the $IN+1$ equations for the $IN+1$ unknowns. Here the terms Φ_n^j, Γ_Q^j, S^i and R^{il} are the discretized versions of the corresponding terms that appear on the right hand sides of (27), (28) and (31). In the algorithm that we have implemented, the unknowns A_n^i are numbered in the order

$$(i=1,\ n=1,2,\ldots,N),\quad (i=2,\ n=1,2,\ldots,N),\ldots$$

with Γ as the last unknown. The equations are ordered in similar fashion (with j and m taking the place of i and n in the above scheme), with (28) as the last equation. In addition to the change of variables mentioned at the beginning of this section, the matrix was pre-conditioned by normalizing the maximum magnitude in each column to 1.

Some comments on this algorithm follow. The weight factors used were

$$\theta_1=\theta_2=1,\quad \theta_3=10^{-6}\text{–}10^{-10}$$

Setting $\theta_3=0$ makes virtually no difference the flow rate, but affects the residual in (31). We have implemented the algorithm in double precision and used a linear equation solver [16] which estimates the condition number of the matrix; despite our attempts at pre-conditioning, the condition numbers are of the order of 10^{13}–10^{17}. The condition number test applied [16] was that the machine should not give the same values for the condition number C and $C+1$, when implemented in double precision. This test did not fail in any of the examples presented in Sections 7 and 8. For a given value of N (typically 4–10 for the examples considered here) some experimentation is needed to fix the optimal values of I, J, K and M. Because of the fairly high condition numbers, the convergence is extremely sensitive to the values of these parameters, as well as those of δ, α and the aspect ratio defined as B/H. It should be emphasized that the exact solution itself is not necessarily sensitive as indicated above. The point is that if the algorithm yields an acceptable solution for a certain combination of parameters, making very small changes in these parameters would tend to make the algorithm fail. A painstaking trial and error procedure would be needed to find a different combination of parameters that work (in the sense described in the ensuing paragraph). Typically, I ranged from 5 to 20; J from 30 to 120; K from 15 to 60; and M from 100 to 200 in the examples presented in the ensuing section. The aspect ratios considered ranged from 1 to 10; the contact angle α, from 0° to 60°; and δ was set at 0.7. Note here that we need to solve the problem for only one value of δ, which may be chosen according to convenience; in actual practice, δ will be very close to 1. The computation times on a Pentium-III personal computer were of the order of a few seconds or minutes; the memory requirements of this algorithm are negligible.

For estimating the convergence of the obtained solutions, the flow rates at various stations in ξ for a given combination of parameters were calculated and compared for equality. The more accurately the no-normal velocity boundary conditions at the free surface and the solid wall are satisfied, the less will be the discrepancy in the calculated flow rates at various ξ. An algorithm that computes these boundary conditions as well as the errors in (31) and (34) was also implemented. Secondly, as N and/or I are increased, the flow rate should exhibit convergence. Finally, the finite difference scheme has a local truncation error of $O([h(1-\delta)]^4)$, as stated in Appendix B. If $I=10$ (which implies $h=1/9$) and $\delta=0.7$, the local truncation error is of the order of 10^{-6}, which is about a couple of orders of magnitude less than those of the computed flow rates; in most cases, this level of accuracy is sufficient in order to obtain excellent results, which are presented in the ensuing section.

7. NUMERICAL RESULTS

We first consider a special solution that is of relevance here. Suppose the harmonic solution in (20) were to vanish identically; that is, $A_n \equiv 0$ for all n. The resulting 'quadratic solution' is given by

$$u_{\mathrm{q}} = \frac{\varepsilon(1-\delta)(\omega^2 - y^2)\lambda\cos\alpha}{4\omega^2}$$

$$v_{\mathrm{q}} = -\frac{\varepsilon^2(1-\delta)^2\lambda\cos\alpha}{12}\left[1 - \frac{y^3}{\omega^3}\right], \quad w_{\mathrm{q}} \equiv 0$$

The leading-order flow rate $\Theta(\xi)(=\varepsilon\Gamma)$ is as defined in (26). The flow rate must, of course, be independent of ξ by continuity. If one now substitutes the quadratic velocity u_{q} into the double integral of (26), the resulting flow rate $\Theta_{\mathrm{q}}(\xi)(=\varepsilon\Gamma_{\mathrm{Q}}(\xi)$; see (29)) would *not* be independent of ξ. The reason is that the quadratic profile does not satisfy the free surface boundary condition (16). The addition of the harmonic correction term in (20) to this quadratic solution should therefore lead to a much better match of the flow rates at various stations than provided by the quadratic solution. This is one of the criteria used to estimate the convergence of the solution. Define the residual (i.e. the left hand side minus the right hand side) of (27), divided by $\varepsilon^2(1-\delta)^2$, as $R_f(\xi, y)$. Define as $R_{f\mathrm{q}}(\xi, y)$ the similarly scaled residual of (27) for the quadratic solution given above. For the quadratic and computed solutions, a comparison of this residual as well as that of the normal velocity $v_t(\xi, z) = v_3(\xi, \omega(\xi), z)/[\varepsilon^2(1-\delta)^2]$ is given at various stations in ξ for the examples presented below (the y- and z-dependence, when it occurs, is handled by taking root mean square over N equally spaced points; only the ξ-dependence is displayed). Note also that the quadratic solution has $v_t \equiv 0$. For all the examples considered in this section, the following values of δ, the channel length L and height H along with the calculated value of ε, were used:

$$\delta = 0.7; \quad L = 0.67\ \mathrm{m}; \quad H = 0.005\ \mathrm{m}; \quad \varepsilon = 0.00878$$

Four values of the contact angle α, namely, 0, 15, 30 and 60°, were considered. It must be kept in mind that for a given propellant and the material of the PMD (usually titanium or

Table I. $\alpha = 0^\circ,\ \beta = 2,\ N = 6,\ J = 60,\ K = 30,\ I = 10,\ M = 100.$

ξ	Θ	Θ_q	R_f	R_{fq}	ζ_0	v_t
0	2.302E − 4	4.181E − 4	2.8E − 4	0.048	−1.8E − 4	2.6E − 4
1/9	2.302E − 4	4.188E − 4	1.9E − 4	0.046	−2.8E − 5	2.8E − 4
2/9	2.302E − 4	4.184E − 4	3.3E − 4	0.045	−1.3E − 5	3.1E − 4
1/3	2.302E − 4	4.170E − 4	8.5E − 5	0.043	9.5E − 6	3.2E − 4
4/9	2.303E − 4	4.147E − 4	2.5E − 4	0.041	2.8E − 4	3.1E − 4
5/9	2.302E − 4	4.113E − 4	1.7E − 4	0.040	−3.8E − 4	4.6E − 4
2/3	2.302E − 4	4.069E − 4	1.5E − 4	0.038	3.9E − 6	4.1E − 4
7/9	2.303E − 4	4.015E − 4	1.3E − 4	0.037	4.8E − 4	2.8E − 4
8/9	2.302E − 4	3.951E − 4	1.2E − 4	0.035	4.4E − 4	4.1E − 4
1	2.301E − 4	3.877E − 4	1.3E − 4	0.033	−3.1E − 4	2.0E − 4

stainless steel), α is a constant (close to zero for most propellants). In the tables that follow, β is the aspect ratio B/H and $\zeta_0(\xi)$ is defined as

$$\zeta_0(\xi) = \psi_0(\xi)/[\varepsilon^2(1-\delta)^2]$$

where ψ_0 is given in (34); note that $\zeta_0(\xi)$ must vanish for the planar solution to exist. The scaling factor of $\varepsilon^2(1-\delta)^2$ chosen for these residuals is more stringent than required; the appropriate scaling factor should be $\varepsilon^2(1-\delta)$, which is the order of magnitude of v_3 and w_3. The ratio $\upsilon = \Theta/\Theta_q(0.5)$ (here Θ can be evaluated at any value of ξ, since it is more or less constant) should always be less than one and should decrease with increasing β for a given contact angle, as noted in Section 4. Two further quantities that appear are defined, for each specific run, as follows:

$$\Theta_d \equiv \text{maximum magnitude of difference in } \Theta(\xi) \text{ between any two grid locations in } \xi$$

$$\Theta_{dq} \equiv \text{maximum magnitude of difference in} \Theta_q(\xi) \text{ between any two grid locations in } \xi$$

Obviously our goal is to demonstrate that $\Theta_d \ll \Theta_{dq}$. Table I shows the results of a simulation for $\alpha = 0^\circ$ and $\beta = 2$. Here the notation aEb means $a \times 10^b$.

Note the excellent agreement of the computed flow rates at various stations in ξ against the relatively poor agreement for the quadratic flow rates. Observe that the residuals in the free surface boundary condition have been reduced by two orders of magnitude as compared to the quadratic case. Importantly, $\zeta_0(\xi)$ does become vanishingly small for all practical purposes, thus guaranteeing the existence of the planar solution. These results are typically true of all runs. Table II shows the values of the scaled coefficients $\tilde{A}_n(\xi)$ (see (38)) obtained for the run of Table I.

Note that the coefficients A_n are indeed slowly varying in ξ. In general, in order to obtain a converged result for some particular A_n, one would need $N \gg n$; the other parameters such as I, M, J and K would also need to be suitably high. Table III illustrates the convergence with respect to N of the flow rate $\Theta(5/9)$ and the first coefficient $\tilde{A}_1(5/9)$, for the same values of $(\alpha,\ \beta,\ I,\ M)$ as in Table I.

Table II. Scaled coefficients $\tilde{A}_n(\xi)$ for the simulation of Table I.

n	$\xi=0$	$\xi=1/3$	$\xi=2/3$	$\xi=1$
1	−0.703397	−0.789624	−0.888838	−0.994018
2	−7.741479	−8.14264	−8.60948	−9.09258
3	−11.04927	−11.42175	−11.71235	−11.80866
4	−13.62433	−14.03890	−13.36747	−11.21748
5	−10.60715	−12.51492	−12.72443	−10.53379
6	−1.71487	−3.28314	−4.10906	−3.80639

Table III. Convergence with respect to N; $\alpha=0^\circ$, $\beta=2$, $I=10$, $M=100$.

N	4	5	6	7	8
J	60	60	60	60	65
K	30	30	30	30	32
$R_f(5/9)$	1.4E − 4	5.3E − 5	1.7E − 4	6.9E − 5	1.2E − 4
$\zeta_0(5/9)$	7.9E − 5	4.1E − 5	−3.8E − 4	−1.7E − 4	8.4E − 4
$v_t(5/9)$	3.5E − 5	1.4E − 4	4.6E − 4	2.0E − 4	3.6E − 4
$\Theta(5/9)$	2.295E − 4	2.282E − 4	2.302E − 4	2.231E − 4	2.370E − 4
Θ_d	1.3E − 7	1.1E − 7	1.4E − 7	1.4E − 7	4E − 7
$\tilde{A}_1(5/9)$	−0.87084	−0.89985	−0.85442	−0.86591	−0.86058
v	0.556	0.553	0.557	0.540	0.574

Table IV. $\alpha=0^\circ$, $\beta=2$.

M	25	100	100	200
I	5	10	20	5
J	30	40	60	120
K	15	20	30	60
N	5	4	6	5
$v_t(0)$	2.7E − 3	7.7E − 4	3.2E − 4	3.1E − 5
$\zeta_0(0)$	1.2E − 3	2.7E − 5	2.0E − 4	2.1E − 4
$R_f(0)$	7.6E − 4	6.3E − 4	2.6E − 4	8.5E − 4
$\Theta(0)$	2.465E − 4	2.329E − 4	2.413E − 4	2.337E − 4
Θ_d	9E − 7	4.4E − 7	2.4E − 7	1.1E − 6
v	0.597	0.564	0.584	0.566

Note that the convergence is fairly satisfactory and that $N=6,7$ produce the best results. In general, the number of Fourier modes (J and K) needs to be increased as N increases. The minimum number of modes required depends on the values of the coefficients A_n, and cannot be easily predicted *a priori*. Table IV lists the flow rate as I, J, K and M are varied in addition to N. The flow rate seems to have converged to within 5% error.

Finally, some results for other aspect ratios and contact angles are presented in Table V.

Table V. Results for different aspect ratios and contact angles.

N	6	6	7	7	6	10
J	60	60	65	65	60	66
K	30	30	32	32	30	32
α°	30	30	0	0	15	60
β	1	2	4	8	2	2
M	100	100	100	100	100	100
I	10	10	10	10	20	20
$\Theta(0)$	1.028E − 4	2.386E − 4	5.572E − 4	1.082E − 3	2.312E − 4	3.999E − 4
Θ_d	1.4E − 7	1E − 7	1.1E − 6	2.6E − 6	2.2E − 7	1.2E − 6
$\Theta_q(0.5)$	1.92E − 4	5.62E − 4	1.15E − 3	2.63E − 3	4.97E − 4	6.6E − 4
Θ_{dq}	8E − 6	1.35E − 4	2.92E − 4	8.1E − 4	8.96E − 5	2.05E − 4
$R_f(0)$	2.2E − 4	3.56E − 4	1.47E − 4	1.63E − 3	6.4E − 4	1.2E − 3
$\zeta_0(0)$	−7.3E − 3	1.9E − 3	−3.8E − 4	−5.5E − 3	−5.1E − 4	1.4E − 3
$v_t(0)$	4.9E − 6	1.7E − 5	6.8E − 4	2.9E − 3	1.0E − 4	3.9E − 5
υ	0.535	0.424	0.485	0.411	0.465	0.606

Note that $\upsilon < 1$ in all instances (see also Tables III and IV) and for given α, υ decreases as β increases, as may be seen for the two cases $\alpha = 0^\circ$ ($\beta = 2, 4, 8$) and $\alpha = 30^\circ$ ($\beta = 1, 2$). These facts (also confirmed by the numerical results of Section 8) support the remarks made at the end of Section 4. An additional interesting phenomenon is worth pointing out. For $\beta = 2$, as α is increased through (0, 15, 30, 60°), one finds from Tables III and V that the respective values of υ are given by (0.557, 0.465, 0.424, 0.606). This behaviour of υ may be explained as follows. As the contact angle increases, the curvature of the free surface decreases and therefore by continuity, the dissipation due to cross-flow effects may be expected to decrease (in view of the slower variations in y and z). But as α increases, the total cross-sectional area increases and this factor tends to increase the dissipation due to cross flow because of the longer spiraling paths traced out by the fluid. Thus one sees a minimum in υ at some positive value of α because of the influence of these two competing factors.

Finally, the criterion for validity of the stated results of this section, namely Equation (36), was checked at the free surface with $\hat{p}$ replaced by $\hat{p}_3$ and found to be satisfactory in all cases.

8. COMPARISON WITH DATA OF DREYER *ET AL.* IN REFERENCES [11, 12]

Here we report the results of two further numerical simulations for the purposes of comparison to the data of Dreyer *et al.* in References [11, 12]. The data taken from Tables I–III and Table V of Reference [12] are as given in Table VI. Here Q is the theoretical flow rate and the contact angle $\alpha = 0^\circ$ for the fluid used, FC-77. Following the procedure of [11, 12], the exit radius of curvature of the free surface was taken as H/2 and that at the inlet (R_0) was calculated from Equation (16) of Reference [12] (or Equation (12) of Reference [11]) as $R_0 = 0.5384$ cm (0.5623 cm) for Run #29 (36) of Table VI. Note that the device used in Table VI corresponds to Figure 2 (i.e. does not have any gradient in channel height) and the contact angle is not maintained by the free surface in the theory of References [11, 12].

Table VI. Theoretical flow rate data of Dreyer *et al.* [11, 12].

Run #	Fluid	H (cm)	B (cm)	L (cm)	ρ (g/cm^3)	μ (poise)	σ (g/s^2)	Q (cm^3/s)
29	FC-77	0.2	2	7.5	1.789	0.0143	13	1.35
36	FC-77	0.2	1	7.5	1.789	0.0143	13	0.655

Table VII. Numerical results by present algorithm.

Run #	υ	$v_t(0)$	$\zeta_0(0)$	$R_f(0)$	Θ_{dq}	$\Theta_q(0.5)$	Θ_d	$\Theta(0)$	Q (cm^3/s)
29	0.427	0.002	−0.003	3.5E − 4	0.0045	0.0071	5.9E − 5	0.0030	0.447
36	0.470	5.7E − 4	−0.002	7.8E − 4	0.0018	0.0032	3.0E − 5	0.0015	0.224

The parameters ε and δ of our algorithm were then computed as $\varepsilon = 0.03615$ (0.03622) and $\delta = 0.4753$ (0.4724) for Run #29 (36) of Table VI; this computation was done by requiring the theoretical pressure drop to match with that in our device. From Section 2.2, the parameter $\varepsilon^2(1-\delta)R_e$, required to be vanishingly small as compared to one, was calculated as 46.7 (47.8) for Run #29 (36).

Thus we conclude that the Reynolds number terms are not negligible. Further, the relatively high value of ε and low value of δ means that the slow variation assumption in the flow direction X also fails; this is not surprising, because the length $L = 7.5$ cm of the device is not large enough for this assumption to hold. For these reasons, our algorithm does not apply for these data. Unfortunately, these are the only data available for comparison purposes (as the author has verified from Dreyer's group).

Table VII shows the results of our simulations for the above data; the notations are as used in Section 7. The flow rates for the two runs are about one-third of those reported in Table VI. This is not surprising, in view of the above remarks. What is interesting is that the flow rates in Table VI exceed even the quadratic limit, given by Q/υ in Table VII. This suggests that the computed pressure drops (i.e. the inlet and exit radii of curvature of the free surface) by the method of [11, 12] may not be accurate. These flow rate data of Dreyer *et al.* are reported to be in agreement with experiment, but unfortunately the experimentally observed pressure drop data (or meniscus curvatures at the inlet and outlet) are not reported in References [11, 12].

It is the author's belief that the computed flow rates in Table VII cannot be far off the mark, *given* the theoretical pressure drops calculated from References [11, 12]. In support of this claim, we cite Jaekle [10], who estimates the friction losses in his equation (16) assuming steady fully developed laminar flow (i.e. the quadratic velocity profile) and then states below:

'Because the flow is not as simple as the above friction term would tend to indicate (due to varying flow area), the true losses can be conservatively estimated to be as high as twice the above approximation. When computational simulations are conducted, two friction estimates should be used: the one above and one twice as large'.

Jaekle's estimate of the friction losses support our computed values of $\upsilon \approx 0.5$ in Table VII as well as in the computations of Section 7. We also observe that the order of magnitude of

the flow rates computed in Table VII agree with the estimate of 0.4 cm^3/s given by Ducret *et al.* [9], although these authors do not give the details of their calculations.

9. CONCLUDING REMARKS

We omit the actual drainage time calculation because it is completely straightforward. Other variants of the proposed algorithm are possible. For example, one could consider still higher-order finite difference schemes and (35) could have a role to play for higher contact angles and/or aspect ratios. The significant advantages gained with the proposed method of this paper are discussed in detail in Section 5. A problem of interest is to include the effects of small gravity as well in the present method. This is straightforward if gravity were to be in the flow direction. But if the gravity force were to be in any other direction, the symmetry of the calculated flows in y and z would be destroyed. In this case the method we have proposed is still applicable; the eigenfunctions and Fourier modes corresponding to other symmetries in y and z must also be included and boundary conditions on the full domain must be considered. The algebraic complications would increase considerably.

APPENDIX A. EXPRESSIONS FOR P_n, Q_n AND R

Define (using appropriate formulae in the main text and omitting functional dependencies; in particular, f is defined by Equation (9)):

$$K_{nj} \equiv \frac{J_{nj}}{\phi_n} - I_{nj}, \quad S_n \equiv \sinh\left[\frac{b\phi_n}{2}\right], \quad C_n = \cosh\left[\frac{b\phi_n}{2}\right]$$

$$\Lambda_j \equiv \sum_{k=1}^{\infty} \frac{D_{kj}}{2k-1} \sin(\phi_k y), \quad L_n \equiv (-1)^n \sum_{j=1}^{\infty} jK_{nj}\Lambda_j \cos(\kappa_j f)$$

$$T_j \equiv \sum_{k=1}^{\infty} D_{kj} \cos(\phi_k y), \quad M_n \equiv (-1)^n \sum_{j=1}^{\infty} K_{nj} T_j \sin(\kappa_j f)$$

$$\beta_n \equiv \frac{(-1)^{n+1}}{2n-1} \sum_{j=1}^{\infty} jJ_{nj}\Lambda_j \cos(\kappa_j f)$$

$$\chi_n \equiv \frac{(-1)^{n+1}}{2n-1} \sum_{j=1}^{\infty} J_{nj} T_j \sin(\kappa_j f)$$

The formulae for P_n, Q_n and R are given by

$$P_n(\xi, y) = -\frac{y}{\phi_n} \sin(\phi_n y) \cosh(\phi_n f) - \frac{32\omega^2 y}{\pi b^2} \beta_n + \frac{8\omega y(-1)^{n+1}}{(2n-1)b\pi} \sum_{j=1}^{\infty} J_{nj} \cos(\kappa_j f)$$

$$- \frac{8\omega\chi_n \sqrt{(\omega^2/\cos^2\alpha) - y^2}}{b\pi} + \frac{8(-1)^{n+1}\omega^2 y S_n}{b\pi^2(2n-1)^2}$$

$$\frac{Q_n(\xi,y)}{1-\delta}=\frac{y}{2\omega}\left[\left\{\frac{\sin(\phi_n y)}{\phi_n}-y\cos(\phi_n y)\right\}\cosh(\phi_n f)-f\sin(\phi_n y)\sinh(\phi_n f)\right]$$

$$-\frac{8yL_n}{b^2}+\frac{2y}{b\omega}(-1)^n\sum_{j=1}^{\infty}[K_{nj}\cos(\kappa_j f)]-\frac{2M_n\sqrt{(\omega^2/\cos^2\alpha)-y^2}}{b\omega}$$

$$+\frac{(-1)^n y}{(2n-1)b\pi}\left[\frac{4S_n}{\phi_n}-bC_n\right]+\frac{1}{2}\left[\omega-\tan\alpha\sqrt{\frac{\omega^2}{\cos^2\alpha}-y^2}\right]\cos(\phi_n y)\cosh(\phi_n f)$$

$$R(\xi,y)=(1-\delta)^2\lambda\cos\alpha\left\{\frac{y}{12}\left[1-\frac{y^3}{\omega^3}\right]+\frac{(\omega^2-y^2)}{8\omega^2}\left[\tan\alpha\sqrt{\frac{\omega^2}{\cos^2\alpha}-y^2}-\omega\right]\right\}$$

APPENDIX B. FINITE DIFFERENCE SCHEME

Consider five equally spaced points x_i, $i=1,2,\ldots,5$, where the spacing is h. Let $g(x)$ be a function and denote $g_i=g(x_i)$, $g_i'=g'(x_i)$, where prime stands for derivative. The five-point interpolation scheme leads to the following expressions for the derivatives:

$$g_i'=\sum_{j=1}^{5}\frac{\Omega_{ij}g_j}{h}$$

where Ω_{ij} is specified by the entry in the ith row and jth column of the following matrix:

$$\Omega=\begin{bmatrix}-\frac{25}{12} & 4 & -3 & \frac{4}{3} & -\frac{1}{4}\\ -\frac{1}{4} & -\frac{5}{6} & \frac{3}{2} & -\frac{1}{2} & \frac{1}{12}\\ \frac{1}{12} & -\frac{2}{3} & 0 & \frac{2}{3} & -\frac{1}{12}\\ -\frac{1}{12} & \frac{1}{2} & -\frac{3}{2} & \frac{5}{6} & \frac{1}{4}\\ \frac{1}{4} & -\frac{4}{3} & 3 & -4 & \frac{25}{12}\end{bmatrix}$$

For our problem, if $(\xi_i,\ i=1,2,\ldots,I)$ represents the uniform discretization in ξ then we use the above scheme to determine $A_n'(\xi_i)$, $i\leqslant 5$; for $i>5$, the five points corresponding to $(\xi_j,\ j=i-4,\ i-3,\ldots,i)$ are used to determine $A_n'(\xi_i)$. The local truncation error in this scheme is easily shown to be $O([h(1-\delta)]^4)$, which is sufficiently small for our purposes. Note that the factor of $(1-\delta)^4$ is included because of the slow variation (in ξ) of the coefficients $A_n(\xi)$, as explained in Section 5.

ACKNOWLEDGEMENTS

US patent application number 09/864522 has been filed on 24 May 2001 by the author's employer IBM on the material of this paper. The author thanks an anonymous referee of this Journal for insisting on a thorough literature survey and for providing several references.

REFERENCES

1. Grove RK. Liquid-propellant management systems with capillary pumping vanes. Patent No. US4733531, 1988.
2. Kerebel A. Liquid storage reservoir with capillary confinement. Patent No. US4553565, 1985.
3. Heureux JML, Grove RK, King RW. Liquid management apparatus for spacecraft. Patent No. US5293895, 1994.
4. Tso-Ping Yeh, Passive propellant management system. Patent No. US4743278, 1988.
5. Qing-peng M, Zhi-jian C, Xiao-gan J and Hong-kun Y. Neutral buoyancy testing method in design of a surface tension tank. *Aerospace Shanghai* 2000; **17**(4):48–51.
6. Kerebel A, Baralle D. A low-cost surface tension tank optimised for telecommunication satellites. *AIAA* 85–1131.
7. Kerebel A, Durgat P. Development of a telecommunications spacecraft propellant tank. *AIAA* 86–1502.
8. Baralle D, Fournier JP. Propellant tank for telecommunication platforms. *AIAA* 89–2761.
9. Ducret E, Le Moullec L, Spencer B, Balaam, P. Propellant management device studies, computational methods and neutral buoyancy tests. *AIAA* 92–3611.
10. Jaekle DE. Propellant management device conceptual design and analysis: Vanes. *AIAA* 91–2172.
11. Dreyer ME, Rosenthal U, Rath HJ. Critical velocities in open capillary flows. *Proceedings of the Fourth Microgravity and Fluid Physics and Transport Phenomena Conference*, Cleveland, Ohio, August 12–14, 1998; 604–609.
12. Dreyer ME, Rosenthal U, Rath HJ. Experimental investigations on flow rate limitations in open capillary vanes. *AIAA* 98–3165.
13. Rosenthal U, Ohlhoff A, Dreyer ME, Rath HJ. Critical velocity in open capillary channel flows. *AIAA* 2001–5021.
14. Shankar PN. The eddy structure in Stokes flow in a cavity. *Journal of Fluid Mechanics* 1993; **250**:371–383.
15. Shankar PN. Three-dimensional eddy structure in a cylindrical container. *Journal of Fluid Mechanics* 1997; **342**:97–118.
16. Forsythe GE, Malcolm MA, Moler CB. *Computer Methods for Mathematical Computations*, Chapter 3, Prentice-Hall: NJ, 1977.

